Zeitschrift für Physik 194, 1—17 (1966)

An X-Ray Interferometer with Bragg Case Beam Splitting and Beam Recombination

U. BONSE* and M. HART**

Department of Materials Science and Engineering, Cornell University, Ithaca, New York, U.S.A.

Physikalisches Institut der Universität Münster, Münster, Germany

H.H. Wills Physics Laboratory, University of Bristol, England

Received February 24, 1966

A new type of X-ray interferometer which uses Bragg case transmission for beam splitting and for beam recombination is described. The principles and special problems of this interferometer are discussed and a strict plane-wave treatment of the interference phenomena is presented. The feasibility of such a device is demonstrated by some interference patterns, obtained with an instrument made from a silicon crystal for use with copper $K\alpha$ radiation and the 220 Bragg reflection. Since, for the operation of the Bragg case interferometer, strong absorption is not essential, such devices may also be more suitable than the previously reported Laue case interferometer[1, 2] for use with neutrons.

1. Introduction

In optical interferometry, the generation and subsequent recombination of two (or more) coherent beams can be accomplished in many different ways, most of which cannot be applied to X-rays because the refractive index of all materials is too close to unity. The only method which has been successfully used so far, splits and recombines X-ray beams by Laue diffraction[1, 2] in a Borrmann crystal ($\mu t > 3$ where μ is the normal absorption coefficient and t is the crystal thickness). In this paper the principles and the experimental operation of another kind of X-ray interferometer in which the beam splitting and beam recombination are achieved by Bragg case diffraction will be described.

---

* Present address: Physikalisches Institut der Universität Münster, 44 Münster, Germany.

** Present address: H.H. Wills Physics Laboratory, Royal Fort, Bristol, England.

2. General Description of the Bragg Case Interferometer

The interferometer and the layout of the beam paths are shown in Fig. 1a and b. As with the Laue case interferometer[1, 2], the necessary stability of alignment is achieved by making the complete instrument from one single crystal block. The two grooves cut in the crystal have equal widths and are cut at an angle φ to the 220 reflecting planes. A thin lamella between the two grooves serves to split and recombine the X-ray beams while the outer surface of each groove is used as a Bragg reflection mirror M (Fig. 1b).

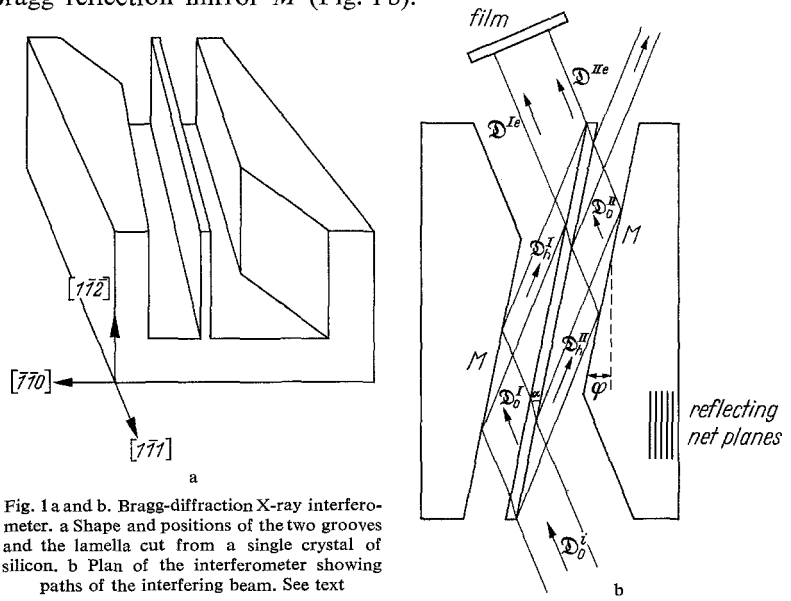

Fig. 1a and b. Bragg-diffraction X-ray interferometer. a Shape and positions of the two grooves and the lamella cut from a single crystal of silicon. b Plan of the interferometer showing paths of the interfering beam. See text

Where the primary beam $\mathfrak{D}_0^i$ is incident on the lamella, the Bragg reflected wave $\mathfrak{D}_h^{II}$ is excited. Inside the lamella a wavefield is set up and will enter the crystal[3] except in the unrealistic case of zero crystal absorption when total reflection can occur. (If total reflection could occur the energy flow of the wavefield inside the crystal would be exactly parallel to the surface.)

The entering angle α of the wavefield (Fig. 1b) may be found from

$$\alpha = \varphi - \beta \tag{1}$$

[1] BONSE, U., and M. HART: Appl. Phys. Letters **6**, 155 (1965); — Z. Physik **188**, 154 (1965).

[2] BONSE, U., and M. HART: Z. Physik **190**, 455 (1966).

[3] BONSE, U.: Z. Physik **177**, 385 (1964).

where β is the angle between the direction $\boldsymbol{j}$ of energy flow and the net planes. β is calculated from*

$$\tan\beta=\frac{R\sin(\vartheta+\varphi)-\sin(\vartheta-\varphi)}{R\sin(\vartheta+\varphi)+\sin(\vartheta-\varphi)}\tan\vartheta \tag{2}$$

where R is the single crystal reflection coefficient and ϑ the Bragg angle. α has a minimum of a few tenths of a degree where the reflectivity R is a maximum. α is largest when no diffraction occurs and the entering wavefield is then just the continuation of the incident wave. Hence $\alpha_{\max}=\varphi+\vartheta$. For the silicon 220 reflection with copper $K\alpha$ radiation, calculated values of the important parameters will be given below, for $\varphi=13.7°$ (the asymmetry actually used in the experiments).

R can be derived from Eqs. (25) and (27) in Ref. [3]. One obtains

$$R(y)=\frac{|\gamma_h|}{\gamma_0}|\xi(y)|^2=E-\sqrt{E^2-1} \tag{3}$$

with

$$E=d^2+f^2+[1+(d^2+f^2)^2-2(d^2-f^2)]^{\frac{1}{2}}, \tag{4}$$

$$d=\frac{v}{|C|}\left|\frac{\chi_{i0}}{\chi_{rh}}\right|\frac{\chi_{ih}}{\chi_{rh}}+y, \tag{5}$$

$$f=\frac{v}{|C|}\left|\frac{\chi_{i0}}{\chi_{rh}}\right|-\frac{\chi_{ih}}{\chi_{rh}}y, \tag{6}$$

$$v=\frac{1}{2}\left(\sqrt{\frac{\gamma_0}{|\gamma_h|}}+\sqrt{\frac{|\gamma_h|}{\gamma_0}}\right). \tag{7}$$

C is the polarisation factor. Since we are concerned only with the weakly absorbed wavefields we will assume throughout the paper that $C=1$ ($\perp$ polarisation state only). y is the parameter which measures the angle of incidence in terms of the range of total reflection in the zero absorption case [Eq. (31′) in Ref. [3]]:

$$y=\left[(\psi_0-\psi_{0B})\sin 2\vartheta\Big/\sqrt{\frac{|\gamma_h|}{\gamma_0}}+|\chi_{r0}|v\right]\Big/|C||\chi_{rh}|. \tag{8}$$**

* This follows immediately from

$$\boldsymbol{j}=[(1+|\xi|^2)\cos\vartheta\boldsymbol{f}-(1-|\xi|^2)\sin\vartheta\boldsymbol{n}]\,[1+|\xi|^4+2|\xi|^2\cos 2\vartheta]^{-\frac{1}{2}}$$

[Eq. (15b) in Ref. [3]] with

$$R=|\xi|^2\frac{|\gamma_h|}{\gamma_0}$$

where, in the usual notation, $\gamma_h=\cos\psi_h$, $\gamma_0=\cos\psi_0$ and ψ_h, ψ_0 are the angles between the surface normal and the $\boldsymbol{K}_h$, $\boldsymbol{K}_0$ wave vectors respectively.

$\xi=D_h/D_0$ is the amplitude ratio of the waves $\mathfrak{D}_h$ and $\mathfrak{D}_0$. $\boldsymbol{n}$ is a unit vector normal to the net planes and $\boldsymbol{f}$ is a unit vector parallel to the net planes and to the plane containing $\boldsymbol{K}_0$ and $\boldsymbol{K}_h$.

** $\psi_{0B}=\pi/2-\vartheta-\varphi$ is the angle of incidence according to the *geometrical* theory of X-ray diffraction.

χ_{r0}, χ_{rh} are proportional to the Fourier coefficients of order 0 and h of the electron density. χ_{i0} and χ_{ih} are proportional to the corresponding Fourier coefficients of the absorptive electron density.

For the beam splitting (and recombining) process it is essential that the internal wavefield reaches the rear surface of the lamella and, while being partially reflected internally, emits the wave $\mathfrak{D}_0^{\mathrm{I}}$ which is necessarily coherent with the wave $\mathfrak{D}_h^{\mathrm{II}}$. Both waves are then surface Bragg reflected at the mirrors M producing the waves $\mathfrak{D}_h^{\mathrm{I}}$ and $\mathfrak{D}_0^{\mathrm{II}}$ (Fig. 1b). In the central lamella $\mathfrak{D}_0^{\mathrm{II}}$ generates a wavefield which is of the same type as that generated by $\mathfrak{D}_0^{\mathrm{I}}$ previously. When this wavefield is partially reflected internally at the rear surface of the upper part of the lamella, the wave $\mathfrak{D}^{\mathrm{II}e}$ will leave the crystal in the region where $\mathfrak{D}_h^{\mathrm{I}}$ generates the surface BRAGG reflected wave $\mathfrak{D}^{\mathrm{I}e}$. Since the waves $\mathfrak{D}^{\mathrm{II}e}$ and $\mathfrak{D}^{\mathrm{I}e}$ are coherent by reason of their formation they will interfere. In particular, as will be shown later, if the geometry is ideal both waves are in phase and will interfere constructively.

3. The Intensities of the Interfering Waves $\mathfrak{D}^{\mathrm{I}e}$ and $\mathfrak{D}^{\mathrm{II}e}$

There are several factors that influence the intensities of the waves $\mathfrak{D}^{\mathrm{I}e}$ and $\mathfrak{D}^{\mathrm{II}e}$. Both waves are formed after two surface Bragg reflections and one Bragg transmission (although the sequence is different for the two waves). Each surface Bragg reflection introduces an intensity factor R while the Bragg transmission introduces two factors $(1-R)$, one from the surface Bragg reflection at the entrance surface and the other from the partial internal reflection at the exit surface of the lamella (see Fig. 4). Absorption of the wavefield within the lamella introduces a factor $\exp[-\sigma_j\, t\, \mathrm{cosec}\,\alpha]$ where t is the thickness of the lamella and σ_j is the absorption coefficient of a wavefield whose flow direction is parallel to the unit vector $\boldsymbol{j}$. Thus the intensity of the beams $\mathfrak{D}^{\mathrm{I}e}$ and $\mathfrak{D}^{\mathrm{II}e}$ is proportional to

$$R^2(1-R)^2 \exp[-\sigma_j\, t\, \mathrm{cosec}\,\alpha].$$

From Eq. (23) of reference [3]

$$\sigma_j = \mu\left(1+|\xi|^2+2C\frac{\chi_{ih}}{\chi_{i0}}\xi_r\right)(1+|\xi|^4+2|\xi|^2\cos 2\vartheta)^{-\frac{1}{2}}. \qquad (9)$$

ξ_r is the real part of $\xi = D_h/D_0$, the amplitude ratio of the component waves $\mathfrak{D}_h$ and $\mathfrak{D}_0$ which make up the wavefield. $\xi(y)$ can be found from Eq. (25) of reference [3]. The absorption is anomalously low if $\xi_r<0$ and anomalously high if $\xi_r>0$ $(C>0)$. The magnitude of the absorption anomaly is essentially determined by the ratio χ_{ih}/χ_{i0}. In the Bragg case interferometer the paths are sufficiently long that only the wavefields with low absorption are important.

It has been shown[3] that in the Bragg case, where complex values of ξ have to be considered, σ_j has its minimum for $\xi_r=-1$. Because $R=|\xi|^2\,|\gamma_h|/\gamma_0<1$, in the Bragg case the condition $\xi_r=-1$ can be realised only if $|\gamma_h|/\gamma_0<1$. This means that the minimum absorption can be obtained with an asymmetry $\varphi>0$ as indicated in Fig. 1 b.

But $\varphi>0$ is also advantageous from another point of view. With $|\gamma_h|/\gamma_0\doteq 0.3$ for example, $\xi_r=-1$ can be obtained with a fairly low value of R, which is equivalent to $\xi_i\ll\xi_r$ (ξ_i is the imaginary part of ξ). Consequently, $|\xi|\simeq|\xi_r|=1$ and the energy flow with minimum absorption will be almost parallel to the reflecting planes (see equation for j in footnote on p. 3), a situation well known in the Laue case of diffraction. On the other hand, in the symmetric ($\varphi=0$) or nearly symmetric ($\varphi>0$ but small) Bragg case, the paths of wavefields with this flow direction inside the crystal are extremely long. Thus with $\varphi=0$ or φ too small the advantage of a low absorption is negated by the increased path length. For these reasons, the interferometer is cut *asymmetrically* with $\varphi=13.7°$ ($|\gamma_h|/\gamma_0=0.286$).

4. Calculation of Bragg Transmission

To confirm these considerations and to obtain an estimate of the *magnitudes* of the intensities of the waves $\mathfrak{D}^{\mathrm{I}e}$ and $\mathfrak{D}^{\mathrm{II}e}$ the following quantities have been calculated:

the single crystal reflection coefficient $R(y)$,
the entering angle $\alpha(y)$ of the Bragg case wavefield,
the absorption anomaly $\sigma_j(y)/\mu$ and
the Bragg transmission coefficient

$$\exp[-\sigma_n(y)\,t] \quad \text{where} \quad \sigma_n(y)=\sigma_j(y)\,\mathrm{cosec}\,\alpha\,.$$

All calculations have been made for the crystal actually used in these experiments, i.e., for the silicon 220 reflection with copper $K\alpha$ radiation, $\varphi=13.7°$ and $t=504$ µm. The results are plotted in Fig. 2 and 3.

Parameters needed in these calculations are χ_{r0}, χ_{i0}, χ_{rh} and χ_{ih}/χ_{i0} where

$$|\chi_{r0}|=\frac{e^2\,\lambda^2}{\pi\,m\,c^2}N \tag{10}$$

(e: electron charge, m: electron mass, λ: X-ray wavelength, N: number of electrons per cm^3, c: light velocity).

For silicon $N=6.990\times10^{23}$ cm^{-3} and with copper $K\alpha$ radiation one calculates $|\chi_{r0}|=1.488\times10^{-5}$.

χ_{i0} is obtained from

$$\chi_{i0}=-\frac{\mu\lambda}{2\pi}. \tag{11}$$

From the International Tables $\mu=141.2$ cm^{-1} whereas experimentally[4] $\mu=144$ cm^{-1}.

[4] Hildebrandt, G.: Private communication.

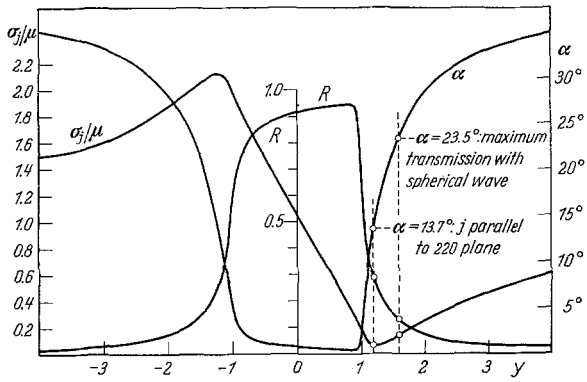

Fig. 2. Calculation of single crystal reflection curve $R(y)$, entering angle $\alpha(y)$ of Bragg case wavefield and absorption anomaly $\sigma_j(y)/\mu$. 220 reflection of silicon, copper $K\alpha$ radiation, angle between surface and reflecting planes $\varphi=13.7°$. Note the transition of σ_j/μ from anomalously high absorption ($y<0.07$) to anomalously low absorption ($y>0.07$). $\alpha_{min}=0.49°$; for large $|y|$, α approaches $\alpha_{max}=\vartheta+\varphi=37.4°$

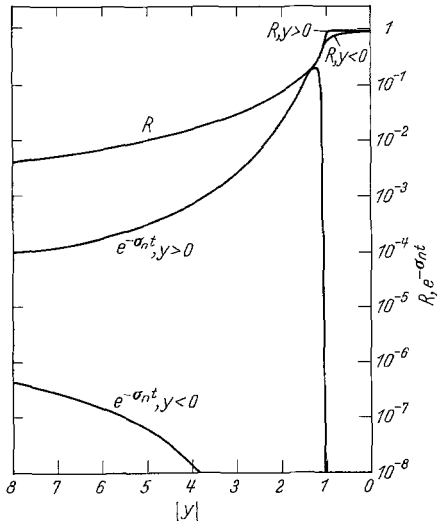

Fig. 3. Bragg transmission coefficient $\exp[-\sigma_n t]$ and $R(y)$, calculated. $\sigma_n=\sigma_j(y)/\sin\alpha$. 220 reflection of silicon, copper $K\alpha$ radiation, $\varphi=13.7°$, $t=504$ μm. Note the stronger dependence of $\exp[-\sigma_n t]$ on the state of absorption as compared with R

We use $\mu=142\ \mathrm{cm}^{-1}$ and calculate $|\chi_{i0}|=3.48\times10^{-7}$.
$|\chi_{rh}|$ was calculated from

$$|\chi_{rh}|=|\chi_{r0}|\frac{f_{220}}{Z}. \tag{12}$$

From recent measurements of the scattering factor f_{220} of silicon which gave[5] $f_{220}=8.59$ at room temperature one obtains $|\chi_{rh}|=9.13\times10^{-6}$. Since no measure-

[5] The mean value of two independent measurements by HART, M.: Z. Physik **189**, 269 (1966) and HATTORI, H., late H. KURIYAMA, T. KATAGAWA, and N. KATO: J. Phys. Soc. Japan **20**, 988 (1965) is used here.

ments of the ratio χ_{ih}/χ_{i0} for the silicon 220 reflection with copper $K\alpha$ radiation have been reported, it was determined by measuring the minimum absorption coefficient $\sigma_{j\,\min}$. From (9) it follows that

$$\frac{\chi_{ih}}{\chi_{i0}} = 1 - \sigma_{j\,\min}\frac{\cos\vartheta}{\mu}. \tag{13}$$

Two silicon wafers $t_1 = 0.180$ cm and $t_2 = 0.279$ cm thick were prepared with surfaces parallel to (111) planes. For each platelet, the anomalously transmitted (diffracted) intensities I_1, I_2 were measured for the symmetric $\bar{2}20$ Laue reflection of copper $K\alpha$ radiation. The tube was operated at only 16 kV so that harmonics were not generated. Since, even for the thinner specimen, $\mu t \simeq 25$, only the wavefields with least absorption contribute to the integrated reflection so that[6]

$$I_2/I_1 = \sqrt{\frac{t_1}{t_2}}\exp\left[-(t_2 - t_1)\,\sigma_{j\,\min}\right]. \tag{14}$$

In this way we obtained the value $\sigma_{j\,\min} = 7.87\ \mathrm{cm}^{-1}$ and, for $\mu = 142\ \mathrm{cm}^{-1}$ the result $\chi_{ih}/\chi_{i0} = 0.949$ is calculated.

As may be seen from Fig. 2, for $y \simeq 0.8$ the reflectivity R has indeed a maximum very close to 1 (R max $= 0.945$). Correspondingly the smallest entering angle of the wavefield is only $\alpha_{\min} = 0.474°$.

In the Bragg case, with the conditions given here, the absorption is anomalously high for $y < 0$ and anomalously low for $y > 0$ (strictly $y < 0.07$ and $y > 0.07$ respectively, see curve σ_j/μ in Fig. 2). The minimum of σ_j is practically as low as in the Laue case ($\sigma_{j\,\min} = 7.87\ \mathrm{cm}^{-1}$ or $\sigma_{j\,\min}/\mu = 0.0554$) and occurs exactly when $\boldsymbol{j}$ is parallel to the 220 planes ($\alpha = 13.7°$, $y = 1.20$, $R = 0.287$).

The absorption anomaly is very strong (Fig. 3). For example, at $y = 1.30$ ($\alpha = 16.9°$) the Bragg transmission coefficient $\exp(-\sigma_n t)$ has its maximum value of 0.207 whereas at $y = -1.30$ the Bragg transmission coefficient is 10^{-23}! Although the maximum Bragg transmission occurs at $y = 1.30$, the minimum value of σ_j occurs at $y = 1.20$. The reason for this shift is the overcompensation of a lower σ_j value by an increased path length as mentioned above. It is also seen from Fig. 3 that considerable intensity is transmitted over a fairly large angular range: $\exp[-\sigma_n t] > 0.1$ for $1.1 < y < 1.55$ which corresponds to $9.1° < \alpha < 23°$.

5. Measurement of the Bragg Transmission

The Bragg transmitted intensity through a lamella of thickness t was measured for a 20 μm wide incident spherical wave (Fig. 4). The ratio of transmitted intensity I_T to incident intensity I_0 is proportional to $(1-R)^2 \exp[-\sigma_n t]$.

[6] KATO, N.: J. Phys. Soc. Japan **10**, 46 (1955).

Inside the crystal the beams are spread over the large angular range $\Delta\alpha \simeq 12°$ while the incident beam is passing through the reflection range $\Delta\psi_0$ of approximately 4 seconds of arc. Therefore a geometric weakening of the intensity per unit area proportional to

$$\left|\frac{d\psi_0}{dl} \cdot L\right|$$

occurs behind the lamella. L is the distance between plate and X-ray source.

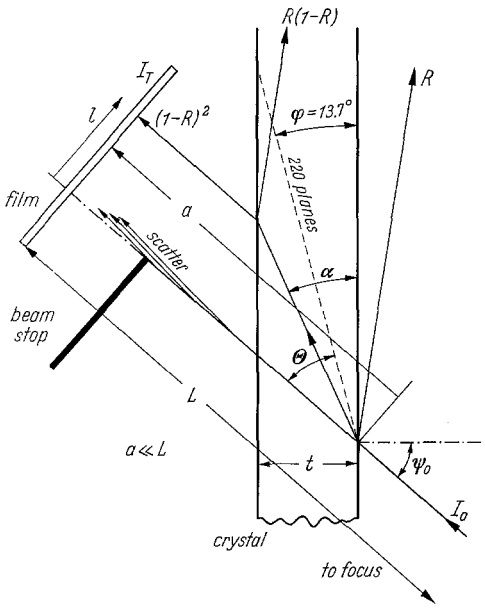

Fig. 4. Lay-out of beams in the case of Bragg transmission of a narrow incident spherical wave. See text for details

In the experiment $L \gg a$ (Fig. 4) and

$$l = t[\operatorname{cotan}\alpha \sin(\vartheta+\varphi) - \cos(\vartheta+\varphi)]. \tag{15}$$

Hence

$$\left|\frac{dl}{d\alpha}\right| = \frac{t\sin(\vartheta+\varphi)}{\sin^2\alpha} = \frac{t\gamma_0}{\sin^2\alpha} \tag{16}$$

with (8) and (16)

$$\begin{aligned} L\left|\frac{d\psi_0}{dl}\right| &= L\left|\frac{d\psi_0}{dy}\right| \cdot \left|\frac{dy}{d\alpha}\right| \cdot \left|\frac{dl}{d\alpha}\right|^{-1} \\ &= \frac{L}{t\gamma_0} \frac{\sqrt{\frac{|\gamma_h|}{\gamma_0}}\,|C|\,|\chi_{rh}|}{\sin 2\vartheta} \left|\frac{dy}{d\alpha}\right| \sin^2\alpha, \end{aligned} \tag{17}$$

or

$$L\left|\frac{d\psi_0}{dl}\right| = 0.608\times 10^{-2}\left|\frac{dy}{d\alpha}\right|\sin^2\alpha \tag{18}$$

if $\frac{L}{t\gamma_0} = 10^3$ is assumed.

The transmitted intensity I_T is now

$$I_T = I_0\times 0.608\times 10^{-2}\left|\frac{dy}{d\alpha}\right|\sin^2\alpha(1-R)^2\exp[-\sigma_n t]\,. \tag{19}$$

I_T was calculated from (19) and has been plotted as a function of l in Fig. 5. The maximum transmission occurs near $y=1.6$ ($\alpha=23.5°$) though the maximum of $\exp[-\sigma_n t]$ occured near $y=1.30$ ($\alpha=16.9°$). This shift is due to the factor $\sin^2\alpha(1-R)^2$ which increases with α. (In the interferometer, the additional factor R^2 will shift the maximum back again by about 5°.) Also shown in Fig. 5 is a microdensitometer

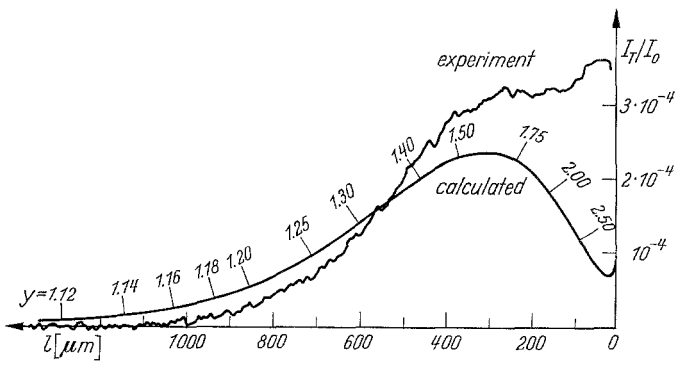

Fig. 5. Comparison of calculated and experimental Bragg transmission of a narrow spherical wave through the silicon lamella $t=504$ μm thick. l: abscissa ⊥ to transmitted beam. 220 reflection, copper $K\alpha$ radiation, $\varphi=13.7°$. Ordinate of densitometer trace normalised to best fit. (Increase of calculated intensity near $l=0$ is due to the factor $L\,d\psi_0/dl$ which tends to 1)

trace of the measured intensity distribution behind the lamella. The ordinate of the measured curve has been normalised for best fit to the calculated one. Except near the incident direction, where the short wavelength component of the incident beam and its scatter predominates, the agreement is quite good. This is the experimental confirmation that energy is indeed transmitted in the Bragg case over a *fairly wide range* $\Delta\alpha$ inside the crystal. This is quite different to the situation in the Laue case interferometer[1,2] where the energy flow is confind to a narrow Borrmann triangle with $\Delta\alpha\simeq 4°$.

6. Experimental Interference Patterns

Interference patterns obtained with the Bragg case interferometer described above are shown in Fig. 6a–c. A plastic wedge with its edge horizontal was put into one of the beams and produces the almost horizontal, high contrast interference fringes illustrated. These interference topographs demonstrate the feasibility of X-ray interferometers with Bragg case transmission beam splitting and beam recombining components.

However, as may be seen in Fig. 6, the interference fringes do not extend over the whole field. In the upper third and lower left corner there are no fringes because the local variations in groove width cause a loss of coherent overlap of the interfering beams. As with the Laue case interferometer, coherence is lost if a certain limit of geometrical inaccuracy is exceeded. Both 220 and 440 Bragg case interferometers have been sucessfully constructed. In an unsuccessful interferometer the groove widths were found to differ by 80–100 μm; as we will see later, this difference is too large for interference to be observed.

The interference topographs in Fig. 6 were obtained using a double crystal arrangement. The first crystal was an asymmetrically cut silicon crystal using the 220 reflection – this provides a wide field and at the same time eliminates the background. This crystal and the interferometer were set like the two crystals of a double crystal diffractometer in the dispersionless (1, −1) position. Their rocking curve was 4 seconds of arc wide. Fig. 6a and c were made with the crystals set halfway up on opposite flanks of the rocking curve while Fig. 6b was made with the crystals set on the peak. It can be seen that the region with good fringe visibility shifts slightly from left to right between these three topographs. This can easily be explained if one remembers that the direction of energy flow inside the crystal varies drastically if the angle of incidence is changed by setting the two crystals at various points on their rocking curve. Since different directions occur it follows that different parts of the grooves are mated in the interfering beams and that, with imperfect geometry, different geometrical path lengths can occur for rays which interfere in the same part of the field. Thus the coherent region can shift in the observed manner.

We will briefly consider the vertical fringes which are particularly distinct in Fig. 6c. They are not related to the interference effect since they occur even if either $\mathfrak{D}_h^{II}$ or $\mathfrak{D}_0^{II}$ is removed by an opaque screen. They do not occur if either $\mathfrak{D}_0^{I}$ or $\mathfrak{D}_h^{I}$ is removed by a screen. The vertical fringes were obtained only in topographs made with beams which were in the *left hand groove*. Furthermore, by reversing the entire ray path, that is by interchanging the position of the film and X-ray source, the

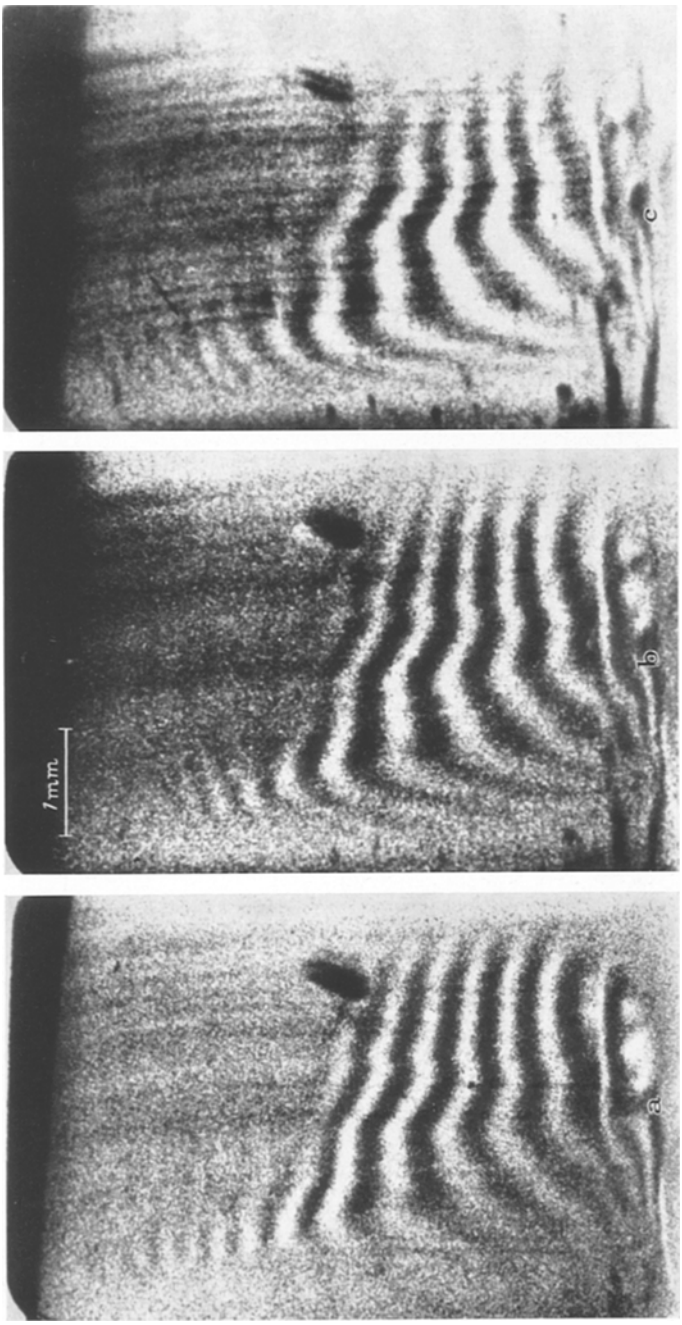

Fig. 6a–c. Interference topographs obtained with a Bragg case interferometer. Double crystal (1, −1) arrangement with asymmetric silicon 220 reflection in front of the interferometer. a set on left flank of Rocking curve. b set on peak of Rocking curve. c set on right flank of Rocking curve. See text for discussion

vertical fringes were observed only in topographs made with beams from the *right hand groove*. To sum up, vertical fringes are only seen with the beam which is first Bragg transmitted and then surface Bragg reflected twice (T.R.R.-beam) and never with the beam which undergoes two Bragg reflections followed by a Bragg transmission (R.R.T.-beam). It is thought that the vertical fringes are images of growth bands which become visible in the last R-reflection of the highly collimated incident TR-beam; the trace of planes normal to the growth axis of the original single crystal is vertical in the topographs of Fig. 6. In the RRT-beam, the wide triangle of energy flow of the final T-reflection completely smears the pattern. It is remarkable that these small lattice parameter variations do *not* appreciably distort the interference pattern whereas in the Laue case interferometer such small deformations are very important[2].

7. Plane Wave Interference Theory

We will assume that the incident wave is the linearly polarised plane wave

$$\mathfrak{D}_0^i = D_0^i \exp[2\pi i(\nu t - \boldsymbol{K}_0^i \cdot \boldsymbol{r})].$$

$\boldsymbol{K}_0^i$ is the wave-vector of the incident wave and $|\boldsymbol{K}_0^i| = k = 1/\lambda$ where λ is the wavelength in vacuum. Outside wave vectors in the direction of the diffracted h waves will be denoted by $\boldsymbol{K}_h^i$. The plane $z=0$ is the mean plane of the lamella, the beam splitter thickness is $2a$ and that of the beam recombiner $2b$ (Fig. 7). Correspondingly, the distance of the mirrors from the plane $z=0$ will be denoted by M_{I} and M_{II}. All waves mentioned in the following calculations are systematically labelled and are indicated in Fig. 7 in the places where they occur in the interferometer. When setting up the boundary condition at a surface for a wave incident from outside of the crystal one only has to consider one wavefield but at a crystal exit surface, where partial internal reflection occurs, wavefields of both type 1 and type 2 must be considered. The amplitude ratios ξ_1 and ξ_2 of any coexistent wavefields must satisfy Eq. (32) in [3].

$$\xi_1 \xi_2 = -\frac{\gamma_0}{\gamma_h} \frac{\chi_h}{\chi_{\bar{h}}} \tag{20}$$

where

$$\xi_1(\psi_0) = D_{h1}/D_{01} \quad \text{and} \quad \xi_2(\psi_0) = D_{h2}/D_{02}. \tag{21}$$

Both ξ_1 and ξ_2 are functions of the incident angle ψ_0 that can be calculated from Eq. (25) in [3]. For simplicity we will assume the existence of an inversion centre so that $\chi_h = \chi_{\bar{h}}$. On the entrance surface $(z=-a)$

of the beam splitter the boundary condition is

$$D_0^i \exp[-2\pi i \boldsymbol{K}_{0z}^i(-a)] = D_{02}^{\mathrm{I}} \exp[-2\pi i \boldsymbol{K}_{02z}^{\mathrm{I}}(-a)], \tag{22}$$

$$D_h^{\mathrm{II}} \exp[-2\pi i \boldsymbol{K}_{hz}^i(-a)] = D_{h2}^{\mathrm{I}} \exp[-2\pi i \boldsymbol{K}_{h2z}^{\mathrm{I}}(-a)] \tag{23}$$

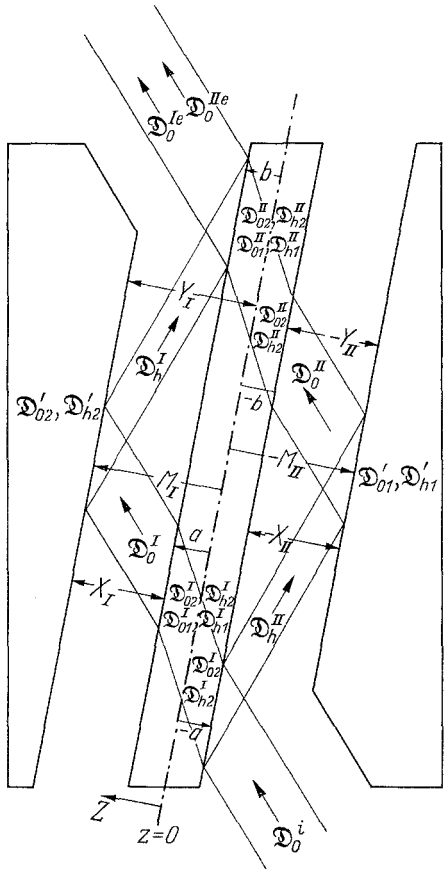

Fig. 7. Waves occurring in the plane wave interference theory of the Bragg case X-ray interferometer

in which the subscript z identifies the z component of a vector. $\boldsymbol{K}_{02}^{\mathrm{I}}$, $\boldsymbol{K}_{h2}^{\mathrm{I}}$ are the wavevectors of the type 2 wavefield that is excited inside the crystal by the incident wave $\mathfrak{D}_0^i$. The type 1 wavefield which is compatible with the above wavefield at the same surface has wavevectors $\boldsymbol{K}_{01}^{\mathrm{I}}$, $\boldsymbol{K}_{h1}^{\mathrm{I}}$. Since the tangential components of the wavevector remain unchanged across a boundary, we can write

$$\begin{aligned} \boldsymbol{K}_0^i - \boldsymbol{K}_{01} &= k\,\delta_1\,z\,, & \boldsymbol{K}_0^i - \boldsymbol{K}_{02} &= k\,\delta_2\,z \\ \boldsymbol{K}_h^i - \boldsymbol{K}_{h1} &= k\,\delta_1'\,z\,, & \boldsymbol{K}_h^i - \boldsymbol{K}_{h2} &= k\,\delta_2'\,z\,. \end{aligned} \tag{24}$$

Here the conventional abbreviations δ_1, δ_2, δ_1', δ_2' have been introduced. Analytical expressions describing the variations of the δ's with the incident angle can be found in VON LAUE's book[7]. For our purpose, it is sufficient to point out that all δ's are of order 10^{-5} to 10^{-6}. With (24) and (22) we find

$$D_{0\,2}^{\mathrm{I}} = D_0^i \exp[+2\pi i k \delta_2 a] \tag{25}$$

and furthermore with (21)

$$D_{h\,2}^{\mathrm{I}} = D_0^i \xi_2 \exp[+2\pi i k \delta_2 a]. \tag{26}$$

This combined with (23) gives

$$D_h^{\mathrm{II}} = D_0^i \xi_2 \exp[-2\pi i k a(\delta_2' - \delta_2)]. \tag{27}$$

At the boundary $z = +a$ two internal wavefields and one outside wave have to be considered. We obtain the conditions

$$\begin{aligned} &D_0^{\mathrm{I}} \exp[-2\pi i \boldsymbol{K}_{0z}^i a] \\ &\quad = D_{01}^{\mathrm{I}} \exp[-2\pi i \boldsymbol{K}_{01z} a] + D_{02}^{\mathrm{I}} \exp[-2\pi i \boldsymbol{K}_{02z} a], \end{aligned} \tag{28}$$

$$0 = D_{h1}^{\mathrm{I}} \exp[-2\pi i \boldsymbol{K}_{h1z} a] + D_{h2}^{\mathrm{I}} \exp[-2\pi i \boldsymbol{K}_{h2z} a]. \tag{29}$$

Using (21) and the Laue equation (30)

$$\boldsymbol{K}_{h1} - \boldsymbol{K}_{01} = \boldsymbol{K}_{h2} - \boldsymbol{K}_{02} = \boldsymbol{h} \tag{30}$$

where $\boldsymbol{h}$ is the diffraction vector of the acting reflection, (28), (29) and (25) can be combined to yield the result

$$D_0^{\mathrm{I}} = D_0^i (\xi_1 - \xi_2) \xi_1^{-1} \exp[4\pi i k \delta_2 a]. \tag{31}$$

At the mirror surface $z = M_{\mathrm{I}}$ in Fig. 7, we have

$$D_0^{\mathrm{I}} \exp[-2\pi i \boldsymbol{K}_{0z}^i M_{\mathrm{I}}] = D_{02}' \exp[-2\pi i \boldsymbol{K}_{02z} M_{\mathrm{I}}], \tag{32}$$

$$D_h^{\mathrm{I}} \exp[-2\pi i \boldsymbol{K}_{hz}^i M_{\mathrm{I}}] = D_{h2}' \exp[-2\pi i \boldsymbol{K}_{h2z} M_{\mathrm{I}}]. \tag{33}$$

Using (21), (24), and (31), with (32) and (33) we find

$$D_h^{\mathrm{I}} = D_0^i \xi_2 \xi_1^{-1} (\xi_1 - \xi_2) \exp\{2\pi i k[(2a - M_{\mathrm{I}}) \delta_2 + M_{\mathrm{I}} \delta_2']\}. \tag{34}$$

By comparing Eqs. (31) and (34) we see that the Bragg reflection at surface $z = M_{\mathrm{I}}$ has introduced an amplitude factor

$$D_h^{\mathrm{I}} / D_0^{\mathrm{I}} = \xi_2 \exp[2\pi i k M_{\mathrm{I}} (\delta_2' - \delta_2)].$$

[7] LAUE, M. v.: Röntgenstrahlinterferenzen. Frankfurt: Akademische Verlagsgesellschaft 1960.

In a similar way the reflection of $\mathfrak{D}_h^{\mathrm{I}}$ into $\mathfrak{D}_0^{\mathrm{I}e}$ at the upper rear surface of the lamella $z=b$ introduces the amplitude factor

$$D_0^{\mathrm{I}e}/D_h^{\mathrm{I}}=\{\xi_1 \exp[2\pi i k b(\delta_1'-\delta_1)]\}^{-1} \tag{35}$$

(in this case the incident wave is an h-wave and the wavefield inside the crystal must be of *type 1* to have an energy flow direction *into the lamella*). Using (34), (30), and (24) it therefore follows that

$$D_0^{\mathrm{I}e}=D_0^i\,\xi_2\,\xi_1^{-2}(\xi_1-\xi_2)\exp\{2\pi i k[2a\,\delta_2+(M_{\mathrm{I}}-b)(\delta_2'-\delta_2)]\}. \tag{36}$$

Notice that (30) and (24) can be combined so that

$$\delta_1'-\delta_1=\delta_2'-\delta_2. \tag{37}$$

Consider now the right hand path (II); the surface Bragg reflection at $z=-M_{\mathrm{II}}$ introduces the amplitude factor [c.f. Eq. (35)]

$$D_0^{\mathrm{II}}/D_h^{\mathrm{II}}=\{\xi_1 \exp[2\pi i k(-M_{\mathrm{II}})(\delta_1'-\delta_1)]\}^{-1} \tag{38}$$

and using (27) and (37) and (38)

$$D_0^{\mathrm{II}}=D_0^i\,\xi_2\,\xi_1^{-1}\exp[2\pi i k(M_{\mathrm{II}}-a)(\delta_2'-\delta_2)]. \tag{39}$$

At the upper front surface of the lamella $z=-b$ the boundary condition requires that

$$D_0^{\mathrm{II}}\exp[-2\pi i \boldsymbol{K}_{0z}^i(-b)]=D_{0\,2}^{\mathrm{II}}\exp[-2\pi i \boldsymbol{K}_{0\,2\,z}(-b)] \tag{40}$$

and using (21), (24) and (39) it follows that

$$D_{0\,2}^{\mathrm{II}}=D_0^i\,\xi_2\,\xi_1^{-1}\exp\{2\pi i k[(M_{\mathrm{II}}-a)(\delta_2'-\delta_2)+b\,\delta_2]\} \tag{41}$$

and

$$D_{h\,2}^{\mathrm{II}}=D_0^i\,\xi_2^2\,\xi_1^{-1}\exp\{2\pi i k[(M_{\mathrm{II}}-a)(\delta_2'-\delta_2)+b\,\delta_2]\}. \tag{42}$$

At the upper rear surface of the lamella $z=b$, partial internal reflection occurs with two internal wavefields and only one external wave $\mathfrak{D}_0^{\mathrm{II}e}$, therefore

$$\begin{aligned} D_0^{\mathrm{II}e}\exp[-2\pi i \boldsymbol{K}_{0z}^i b] \\ =D_{0\,1}^{\mathrm{II}}\exp[-2\pi i \boldsymbol{K}_{0\,1\,z} b]+D_{0\,2}^{\mathrm{II}}\exp[-2\pi i \boldsymbol{K}_{0\,2\,z} b], \end{aligned} \tag{43}$$

$$0=D_{h\,1}^{\mathrm{II}}\exp[-2\pi i \boldsymbol{K}_{h\,1\,z} b]+D_{h\,2}^{\mathrm{II}}\exp[-2\pi i \boldsymbol{K}_{h\,2\,z} b]. \tag{44}$$

Combining (43) and (44) and using (21), (24) and (30), the amplitude of the wave $\mathfrak{D}_0^{\mathrm{II}e}$ is

$$D_0^{\mathrm{II}e}=D_{0\,2}^{\mathrm{II}}\,\xi_1^{-1}(\xi_1-\xi_2)\exp[2\pi i k b\,\delta_2] \tag{45}$$

and with (41) we obtain

$$D_0^{\mathrm{II}\,e}=D_0^i\,\xi_2\,\xi_1^{-2}(\xi_1-\xi_2)\exp\{2\pi i k[2b\,\delta_2+(M_{\mathrm{II}}-a)(\delta_2'-\delta_2)]\}. \quad (46)$$

Finally, from (36) and (46) we obtain the amplitude ratio of the two interfering waves $\mathfrak{D}_0^{\mathrm{I}e}$ and $\mathfrak{D}_0^{\mathrm{II}e}$

$$D_0^{\mathrm{I}e}/D_0^{\mathrm{II}\,e}=\exp\{2\pi i k[\delta_2'(y_{\mathrm{I}}-x_{\mathrm{II}})+\delta_2(y_{\mathrm{II}}-x_{\mathrm{I}})]\} \quad (47)$$

where

$$y_{\mathrm{I}}=M_{\mathrm{I}}-b\,,\qquad y_{\mathrm{II}}=M_{\mathrm{II}}-b\,,$$

$$x_{\mathrm{I}}=M_{\mathrm{I}}-a\,,\qquad x_{\mathrm{II}}=M_{\mathrm{II}}-a\,.$$

It is seen that the waves $\mathfrak{D}_0^{\mathrm{I}e}$ and $\mathfrak{D}_0^{\mathrm{II}\,e}$ are exactly in phase if the dimensions of the interferometer are "ideal", that is if

$$a=b \quad \text{and} \quad M_{\mathrm{I}}=M_{\mathrm{II}}. \quad (48)$$

Furthermore a split-lamella design analogous to the split-mirror Laue case interferometer[8] can be used since (47) requires only that $y_{\mathrm{I}}=x_{\mathrm{II}}$ and $y_{\mathrm{II}}=x_{\mathrm{I}}$ for constructive interference. As has already been pointed out, since δ_2' and δ_2 are both of order 10^{-5} to 10^{-6}, deviations from the ideal geometry by 1 to 10 microns are permissible so that the construction of actual interferometers is not too difficult. Similar results have been obtained for Laue case interferometers[2].

It is also important that with perfect or almost perfect geometry the phase relationship between the exit beams $\mathfrak{D}_0^{\mathrm{I}e}$ and $\mathfrak{D}_0^{\mathrm{II}\,e}$ does not depend on ξ and hence depends neither upon the incident angle ψ_0 nor on the angle of the flow direction α inside the lamella. Thus the calculated phase relationship is also correct for spherical waves.

Let us now consider the effect of the internally reflected wavefields on the interference of the main or first order beams. From Eq. (20) we conclude that in the Bragg case ($\gamma_0/\gamma_h<0$) the coexisting wavefields of type 1 and 2 have the *same* absorption state since the signs of the real parts of ξ_1 and ξ_2 are the same. (This is just the opposite of the situation in the Laue case.) Therefore the partially reflected wavefield generated by a weakly absorbed wavefield at the rear surface of the lamella could in principle again reach the front surface of the lamella and thus generate more waves. With X-rays it is unlikely that the wavefield will have an appreciable energy after penetrating the lamella twice. Furthermore, if it was still sufficiently strong to produce a second system of waves no difficulties would arise because the two system of waves

[8] BONSE, U., and M. HART: Appl. Phys. Letters **7**, 99 (1965).

are spatially separated. Thus the second system of waves could be either utilised or eliminated by suitable screens.

Finally, an important difference between Laue and Bragg case interferometers should be pointed out. Laue case interferometers, as previously described[2], make essential use of the presence of the strong absorption and probably would not work if there was no Borrmann effect. In interference patterns obtained with Laue case interferometers, the dark regions are dark because the energy is dissipated by photoelectric absorption. On the other hand, when destructive interference occurs between the exit beams $\mathfrak{D}_0^{Ie}$ and $\mathfrak{D}_0^{IIe}$ of a Bragg case interferometer, the energy is diverted into the two type 1 wavefields which propagate into the beam recombining crystal from the surface $z=b$. These two wavefields are made up of the pair of internal waves (not entered in Fig. 7) excited by the wave $\mathfrak{D}_h^{I}$ and the pair of waves $\mathfrak{D}_{0\,1}^{II}$ and $\mathfrak{D}_{h\,1}^{II}$ resulting from the partial internal reflection of $\mathfrak{D}_{0\,2}^{II}$ and $\mathfrak{D}_{h\,2}^{II}$ at the surface $z=b$. Thus the energy is *deviated rather than absorbed* when desctructive interference occurs in a Bragg case interferometer. It seems then that this type of interferometer would work *without strong absorption* though multiple internal reflections in the lamella would then be possible. Since it is difficult to obtain suitably perfect, highly absorbing crystals for neutron diffraction, the Bragg case design might be particularly suitable for neutron interferometry.

This work was supported in part by the Advanced Research Projects Agency through the Materials Science Center of Cornell University.